# Active control of the hinge of a flapping wing with electrostatic sticking to modify the passive pitching motion

Peters, H.J.; Wang, Qi; Goosen, Hans; van Keulen, Fred

**Important note**
To cite this publication, please use the final published version (if applicable).
Please check the document version above.

# Chapter 8
# Active Control of the Hinge of a Flapping Wing with Electrostatic Sticking to Modify the Passive Pitching Motion

**Hugo Peters, Qi Wang, Hans Goosen and Fred van Keulen**

**Abstract**  Wing designs for Flapping Wing Micro Air Vehicles (FWMAVs) might use a properly tuned elastic hinge at the wing root to obtain the required passive pitching motion to achieve enough lift production to stay aloft. Practical use of this type of FWMAVs requires some form of control which can be achieved by actively adjusting the elastic hinge stiffness and, thus, the pitching motion and lift production of the wing. This paper studies an elastic hinge design consisting of stacked layers which can be sticked together using electrostatics. This sticking changes the bending stiffness of the hinge. The voltage-dependent behavior of this elastic hinge during the large pitching motion are described in detail. The passive pitching motion is governed by the equation of motion which is a function of the elastic hinge stiffness and the applied control voltage. The lift generated by the passive pitching wings is predicted by a quasi-steady aerodynamic model. Numerical simulations show significant changes of the passive pitching motion and, consequently, of the lift production, if slipping stacked layers stick together. Experiments are conducted to study the practical applicability of this method on FWMAVs. The experiments show similar trends as the numerical simulations in modifying the pitching motion although the effect is less significant which is mainly due to manufacturing difficulties. This approach is, in conclusion, promising to control FWMAV flight.

H. Peters · Q. Wang (✉) · H. Goosen · F. van Keulen
Delft University of Technology, Mekelweg 2, 2628 CD Delft, The Netherlands
e-mail: q.wang-3@tudelft.nl

H. Peters
e-mail: h.j.peters-1@tudelft.nl

H. Goosen
e-mail: j.f.l.goosen@tudelft.nl

F. van Keulen
e-mail: a.vankeulen@tudelft.nl

## 8.1 Introduction

The design and realization of lightweight Flapping Wing Micro Air Vehicles (FWMAVs) have attracted much attention over the last decades. Potential applications of FMWAV designs are in, among others, surveillance (e.g., police and security) and inspection of inaccessible or dangerous locations (e.g., disaster scenes and sewers). The design and realization of FWMAVs is complicated by weight constraints as a result of the limited lift production of the wings. Consequently, designers aim for lightweight, smart and highly integrated systems. This has resulted in several ways of achieving flapping kinematics for sufficient lift production. To decrease the actuation mechanism complexity, some wing designs integrate elastic hinges that allow the wing pitching motion to be passive during the flapping motion [3, 22]. Due to the inertial and aerodynamic loading, a properly tuned elastic hinge results in the required pitching motion to achieve enough lift production to stay aloft.

For stable flight and maneuvering, FWMAV designs require some form of control. In fact, constant control will be necessary because of the intrinsic dynamic instability of the designs. Recent work on the Harvard Microrobotic Fly (i.e., a FWMAV design which exploits passive pitching) applied aerodynamic dampers for stabilization [17], complex mechanisms to induce asymmetric flapping wing kinematics to produce control torques [7], and separate actuators for each wing [11]. Additionally, control torques were created by integrating a piezoelectric bimorph actuator in the wings' elastic hinge to induce a bias during the wing stroke [18]. To control lightweight FWMAV designs, actively adjusting the dynamic properties (i.e., structural damping and stiffness) of the wings' elastic hinge appears to be a promising, elegant, and integrable approach to change the passive pitching motion during flight and, hence, the stroke-averaged lift force. This control approach is not well established within literature.

To actively change the dynamic properties of the wings' hinge, the elastic hinge needs to be replaced by an active hinge which properties change due to some external stimuli (e.g., an electric field). Methods to actively change the dynamic properties of an elastic element are, for example: (i) smart fluids (i.e., magnetorheological or electrorheological fluids) for which the properties transform rapidly upon exposure to an external magnetic or electric field [12], (ii) piezoelectric polymer films (e.g., PVDF) for which the properties change as a function of the connected electrical circuit [4], and (iii) sticking stacked layers using, for example, electrostatics [2, 15].

This paper investigates the method with the stacked layers for which the conceptual idea is shown in Fig. 8.1. Figure 8.1a shows a capacitor-like clamped-free beam which consists of two layers which can slide with respect to each other when deflected by the end-load $F$. Each layer consists of a conducting layer (e.g., steel) and a dielectric layer (e.g., Mylar). Figure 8.1b shows that, during deflection, the two layers slip with respect to each other if the applied voltage $V = 0$. For a specific voltage $V_{st}$, the electrostatic loading causes the layers to stick to each other during deflection, see Fig. 8.1c. Whenever these layers stick, the second moment of area increases, which effectively increases the bending stiffness of the beam.
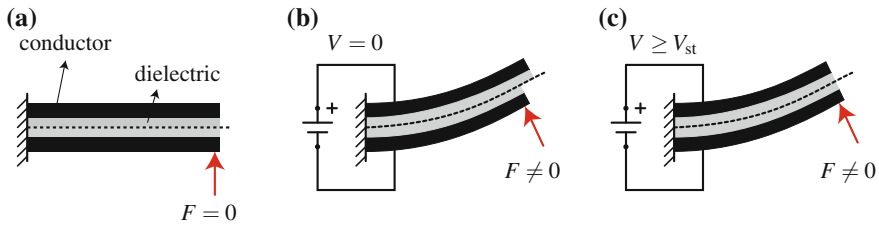
**Fig. 8.1** Conceptual idea to change the bending stiffness of stacked layers. **a** Capacitor-like clamped-free beam with end-load $F$. **b** For $V = 0$, the layers slip with respect to each other during deflection. **c** For $V \geq V_{st}$, the layers stick together which effectively increases the bending stiffness

This work aims to actively control the wing's passive pitching motion by sticking stacked layers using electrostatics. These stacked layers need to be integrated into a lightweight wing design (i.e., total wing design is about 200 mg) and should allow for large passive pitching deflections. This study investigates the influence of electrostatics on the dynamic properties of this active hinge during these large deflections. The wing is assumed to be a thin, rigid plate for simplicity. This work uses a quasi-steady aerodynamic model to obtain the equation of motion of the passive pitching motion as a function of the elastic hinge properties. Experiments are conducted to study the practical applicability of this active element for small-scale and lightweight FWMAV applications.

This paper is organized as follows. Section 8.2 introduces a flapping wing design and the description of the flapping kinematics with, in particular, the passive pitching motion. The theory of the electrostatically controlled structural properties of the elastic hinge is discussed in Sect. 8.3. Section 8.4 presents the equation of motion of a passive pitching flapping wing as a function of the elastic hinge stiffness and the applied control voltage. Section 8.5 discusses the realization of the active hinge, the experimental setup, the obtained measurement results, and a comparison with analytical results. Section 8.7 gives conclusions and recommendations for further research.

## 8.2 Passive Pitching Flapping Motion

### 8.2.1 Flapping Wing Design

Both insects and FWMAVs show flapping wings with different outlines, stiffness distributions and materials. Generally, the pitching motion is partly generated passively with the help of wing flexibility. This wing flexibility can, for instance, be realized with: (i) a flexible veins-membrane structure as known from insect wings [6], (ii) a carbon-fiber-reinforced polymer film as commonly used in FWMAV wing designs
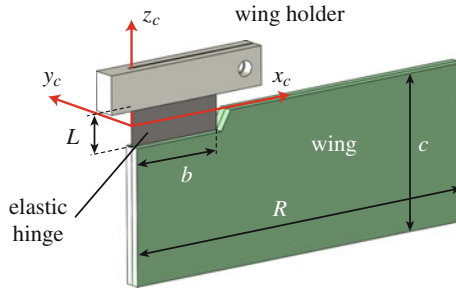
**Fig. 8.2** Schematic drawing of the wing design for a zero pitching angle with the elastic hinge connecting the wing holder to the wing
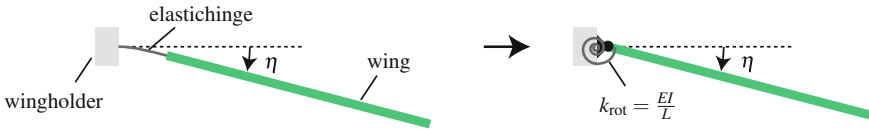


**Fig. 8.3** Side-view sketch of the wing design, rotated through an angle $\eta$, showing the replacement of the compliant elastic hinge with length $L$ by a rotational spring with stiffness $k_{\mathrm{rot}}$

[5], or (iii) an elastic hinge at the wing root to represent the wing stiffness [21]. This work uses the latter approach which is generally used for experimental studies.

Figure 8.2 shows the wing design as studied in the present work, consisting of a rectangular, thin plate which is assumed to be rigid. The mass distribution over the wing surface is assumed to be uniform. Since the focus of the current work is primarily on the active hinge design, such a simple wing layout design is justified. The wingspan and chord length are denoted by $R$ and $c$, respectively. The elastic hinge is located at the wing root and has width $b$, length $L$ and thickness $t$. This elastic hinge is essentially a compliant hinge, which is primarily loaded in bending. The effective rotational stiffness can, consequently, be given by [10]:

$$k_{\mathrm{rot}} = \frac{EI}{L},\qquad(8.1)$$

where $E$ and $I$ are the Young's modulus and second moment of area of the hinge, respectively. Figure 8.3 shows a schematic side-view of the wing design which is rotated through an angle $\eta$ to visualize the result of replacing the compliant elastic hinge with length $L$ by a rotational spring with stiffness $k_{\mathrm{rot}}$. For pure bending, this simple equation is accurate for large deflections. Although the loading of the elastic hinge is more complex during the flapping motion, Eq. (8.1) is assumed to hold during the entire flapping cycle.

## 8.2.2  Passive Pitching and Wing Kinematics

The flapping wing motion is a spatial wing movement that can be decomposed into three successive motions, namely sweeping motion (or yaw), pitching motion (or pitch), and heaving motion (or roll). The sweeping motion drives the wing to sweep reciprocally in a stroke plane with a specified stroke amplitude. The pitching motion controls the geometrical angle of attack (AOA) of the flapping wings. For flapping wings, the highest AOA (i.e., 90°) is, generally, experienced during wing reversal phases while the lowest AOA shows up during the middle of the strokes. The heaving motion represents the out-of-stroke-plane movement which amplitude is generally one order smaller than for the other two motions. Hence, it is ignored in this study. Therefore, the flapping kinematics can be fully determined by the sweeping motion and the pitching motion.

Two Euler angles are used to quantify the wing kinematics: the sweeping angle $\phi$, and the pitching angle $\eta$, as shown in Fig. 8.4. The pitching angle $\eta$ is visualized in Fig. 8.3. Additionally, two coordinate frames are specified which are of particular interest for the study of flapping wing motion: the fixed inertial frame $x_i y_i z_i$ and the co-rotating frame $x_c y_c z_c$ which co-rotates with the wing (see Fig. 8.2). The angular velocity and acceleration of a flapping wing in the co-rotating frame can be expressed by

$$\boldsymbol{\omega}_c = \left[\dot{\eta}, \dot{\phi}\sin(\eta), \dot{\phi}\cos(\eta)\right]^{\mathrm{T}}, \tag{8.2}$$

$$\text{and} \quad \boldsymbol{\alpha}_c = \dot{\boldsymbol{\omega}}_c = \left[\ddot{\eta}, \dot{\phi}\dot{\eta}\cos(\eta) + \ddot{\phi}\sin(\eta), \ddot{\phi}\cos(\eta) - \dot{\phi}\dot{\eta}\sin(\eta)\right]^{\mathrm{T}}, \tag{8.3}$$

respectively. The AOA can be simply obtained by $\|90° - \eta\|$. The inertial and aerodynamic load can be fully determined if Eqs. (8.2) and (8.3) are known. For a given prescribed sweeping motion $\phi(t)$, the tuned elastic hinge stiffness fully determines the (passive) pitching motion and, therefore, the aerodynamic load generation (e.g.,

**Fig. 8.4**  Visualization of the flapping kinematics determined by the sweeping angle $\phi$ and pitching angle $\eta$. Additionally, the fixed inertial frame $x_i y_i z_i$ and the co-rotating frame $x_c y_c z_c$ are shown
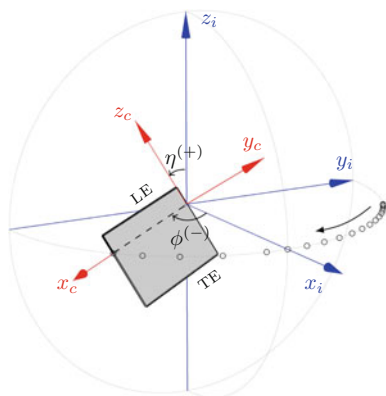
lift force). Consequently, changing the elastic hinge stiffness in an active manner would lead to changes in the aerodynamic load generation and, hence, to a way to control FWMAV flight.

## 8.3 Electrostatically Controlled Hinge Theory

This section discusses a model to electrostatically control the dynamic properties of the active hinge. First, it presents the proposed hinge design followed by a description of the voltage-induced normal stress between the stacked layers. Subsequently, it describes the voltage-dependent behavior during the flapping motion (i.e., whether the layers slip or stick). After that, the voltage-dependent properties of the active hinge (i.e., its rotational stiffness and power dissipation) during the flapping motion are presented.

### 8.3.1 Proposed Elastic Hinge Design

The elastic hinge in the wing design of Fig. 8.2 is replaced by an active hinge for which an enlarged side-view is shown in Fig. 8.5a. The hinge is symmetric in thickness direction. The hinge has length $L$ and width $b$. It consists of a conducting core which is covered on both sides by dielectric layers and two conducting facings. The core connects the wing holder to the wing while the two facings are attached to the wing holder only. The two facings can slide with respect to the core. The thickness of the core, the dielectric layers, and the facings are denoted by $t_c$, $t_d$, and $t_f$, respectively (see Fig. 8.5b). Two clamps are attached to the wing to prevent the layers from separating during the pitching motion. Hence, all layers will always contribute to the resulting bending stiffness. The facings are assumed to slip freely with respect to the clamps.
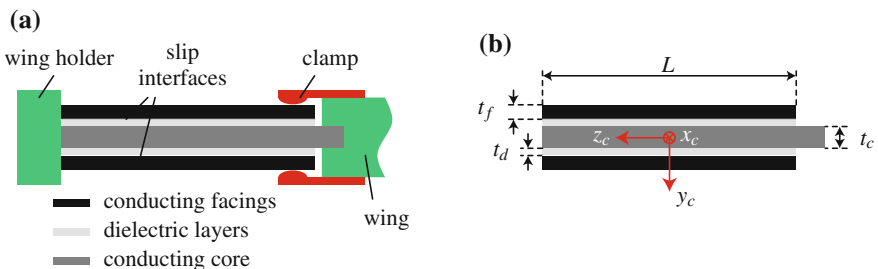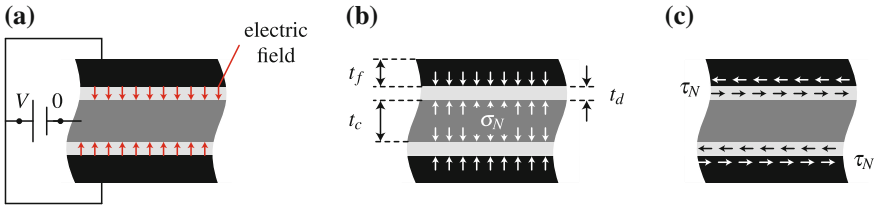


**Fig. 8.5** Symmetric active hinge design. **a** Side-view. **b** Dimensions

**Fig. 8.6** Zoom-in of the active hinge during electrostatic loading. **a** Electric field over dielectric layer due to applied voltage $V$. **b** Normal stress $\sigma_N$ due to the electrostatic loading. **c** Shear stress distribution $\tau_N$ at the interface

### 8.3.2 Voltage-Induced Stresses Between Stacked Layers

By applying a voltage $V$ to the conducting facings of the active hinge while connecting the conducting core to ground, an electric field is created over the dielectric layers, see Fig. 8.6a. This electric field induces a normal stress at the interface between the facings and the dielectric layers, see Fig. 8.6b, which is given by [2]

$$\sigma_N(V) = \frac{1}{2}\frac{\varepsilon_0\varepsilon_r V^2}{t_d^2},\tag{8.4}$$

where $\varepsilon_0$ represents the vacuum permittivity and $\varepsilon_r$ is the material-dependent relative permittivity. The normal stress depends quadratically on the applied voltage $V$ and inversely quadratic on the gap between the conducting layers (i.e., the dielectric layer thickness $t_d$). The normal stress introduces friction between the stacked layers to resist slip during deflection. The shear stress that can be transferred from one layer to the other due to this friction, see Fig. 8.6c, is given by

$$\tau_N(V) = \mu\sigma_N(V),\tag{8.5}$$

where $\mu$ represents the material-dependent friction coefficient at the interface which depends on whether there is relative displacement at the interface (i.e., dynamic friction) or not (i.e., static friction). The sticked layers start to slip with respect to each other if the shear stress at the interface due to deflection becomes higher than the friction-induced shear stress of Eq. (8.5). Thus, Eq. (8.5) determines the threshold value at which the transition from stick to slip at the interface takes place. This work assumes the static and dynamic friction coefficient to be equal to improve the understanding of the active hinge behavior.

### 8.3.3 Behavior of the Active Hinge During Large Deflections

This section describes the stick-slip phenomena of the active hinge as a function of the applied voltage $V$ during large deflections to understand its rather complex behavior (i.e., the active hinge is not a simple spring anymore). The hinge deflects according to the wing pitching motion $\eta(t)$ and it is assumed that the stacked layers slip over the entire interface without restriction for $V = 0$. For $V > 0$, the voltage-induced normal stress tries to prevent slip by introducing friction. The required friction to prevent slip increases if the hinge deflection increases. The required voltage to stick the layers together up to the maximal deflection is denoted by $V_{st}$ (i.e., the layers do, in that case, not slip throughout the entire pitching motion). In the following, two phases are distinguished: the layers either completely slip or completely stick over the entire interface.

Figure 8.7 shows conceptual steady-state stick-slip behavior of the hinge layers during a pitching motion $\eta(t)$ for a voltage $0 < V < V_{st}$. The essential step in understanding the hinge behavior is the investigation of the interface shear stress $\tau_{in}$ during the pitching motion. It is assumed that, at the start of the graph, $\eta$ increases (i.e., deflection increases) and the layers slip. During slip, the interface shear stress $\tau_{in}$ is constant and equal to the friction-induced threshold shear stress (i.e., $\tau_N(V)$). The constant interface shear stress results in a constant shear deformation of the layers, see State 1 in Fig. 8.8. The layers continue to slip until the maximum pitching angle
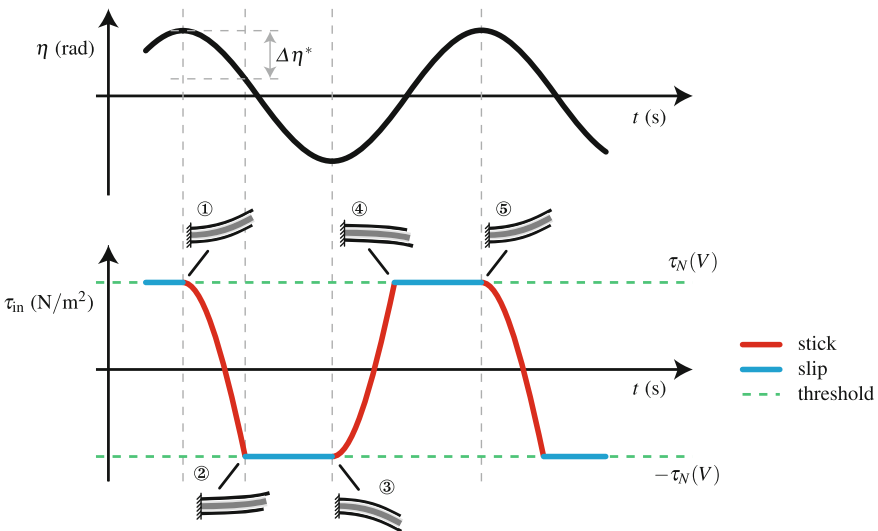


**Fig. 8.7** Conceptual steady-state stick-slip behavior of the voltage-controlled active hinge during the pitching motion $\eta(t)$ for a voltage $0 < V < V_{st}$ with the corresponding interface shear stress $\tau_{in}$. Additionally, it shows the pitch-duration $\Delta\eta^*$ for which the layers stick together. The *dotted green line* represents the friction-induced threshold shear stress $\tau_N(V)$. Characteristic layer off-set configurations are indicated by Configurations 1–5
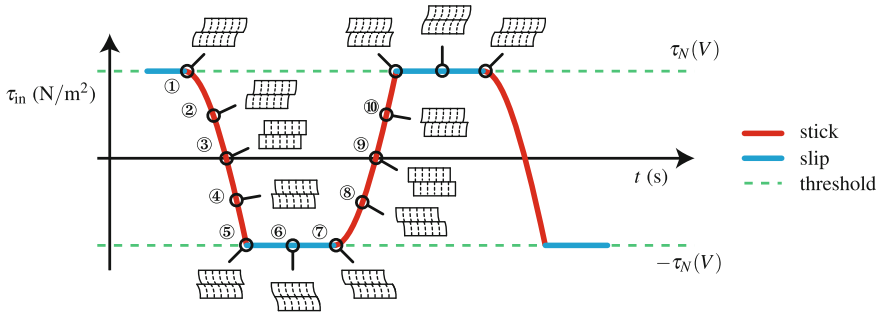
**Fig. 8.8** Sketches of the shear deformation of two layers of the voltage-controlled active hinge during the pitching motion $\eta(t)$ for a voltage $0 < V < V_{st}$ at different interface shear stress values $\tau_{in}$. States 1–10 represent characteristic shear deformation sketches

(i.e., maximum hinge deflection) is reached, resulting in a hinge layer off-set, see Configuration 1 in Fig. 8.7.

There is no relative motion at the interface at the maximal pitching angle, which initiates stick between the layers. At the start of the reversal motion (i.e., $\eta$ decreases), the layers remain sticking since the interface shear stress $\tau_{in}$ becomes lower than the friction-induced threshold shear stress $\tau_N(V)$. The interface shear stress decreases during this reversal until $\tau_{in} = -\tau_N(V)$ (i.e., until the maximum friction-induced shear stress $\tau_N$ is reached again). At that point, the layers have not slipped yet as illustrated by Configurations 1 and 2 in Fig. 8.7 where the layer off-set did not change. The shear deformation of the layers changes according to the changing interface shear stress as represented by States 1–5 in Fig. 8.8. During the remainder of the reversal motion (i.e., until the maximum negative $\eta$), the layers slip and result in a layer off-set opposite to the one at the start of the pitching reversal, see Configuration 1–3 in Fig. 8.7. During this slip, the interface shear stress and, hence, the shear deformation is constant, see States 5–7 in Fig. 8.8.

Thereafter, a similar but opposite cycle starts followed by identical consecutive cycles. If the layers stick, the off-set between the layers remains the same (see, for example, Configuration 3 and 4 in Fig. 8.7) while the interface shear stress and, consequently, the layer shear deformation changes (e.g., States 7–10 in Fig. 8.8). On the other hand, if the layers slip, the off-set changes (e.g., from Configuration 4 to 5 in Fig. 8.7) while the interface shear stress and, consequently, the layer shear deformation, is constant. The complexity that might be caused by the marginal off-set between stacked layers (e.g., buckling), is neglected.

During sticking, the interface shear stress $\tau_{in}$ changes with an amplitude of $\Delta\tau_{in} = 2\tau_N(V)$ before the layers start to slip again as shown by the difference between the horizontal dashed threshold lines in Fig. 8.8. The pitch-duration for which the layers stick is denoted by $\Delta\eta^*$, see Fig. 8.7. To determine $\Delta\eta^*$, the relation between the change of the pitching angle $\eta$ (i.e., $\Delta\eta$) and the known change of the interface shear stress (i.e., $\Delta\tau_{in}$) is used. This relation is clarified in the following based on the flowchart of Fig. 8.9 and the sketches of Fig. 8.10.

**Fig. 8.9** Graphical interpretation of the relation between the change of the pitching angle $\Delta\eta$ and the interface shear stress $\Delta\tau_{in}$. $\Delta P$ and $\Delta Q$ represent the change of the external load on the wing and the shear force at the cross-section, respectively
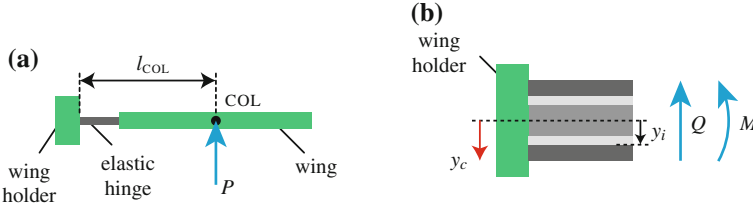


**Fig. 8.10** Side-view sketches of the wing design to determine the interface shear stress, $\tau_{in}$, and pitch angle, $\eta$, due to the external load $P$. **a** center of load (COL) with the external load $P$. **b** zoom-in of the active hinge with moment $M$ and shear force $Q$ at the cross-section due to load $P$

Firstly, the change of the pitching angle $\Delta\eta$ is discussed. During flapping flight, the wing loading can be captured by an external load $P$ which is assumed to remain perpendicular to the wing surface (see Fig. 8.10a) for all angles of attack. This assumption is justified since the strength of the bound circulation at a post-stall angle of attack, that results in a net force perpendicular to the incoming flow, is negligible as compared to the vorticity-induced circulation that results in the load perpendicular to the wing surface [8]. Although the location of the center of load (COL) varies slightly during a flapping cycle we assume it to be constant at a distance $l_{COL} = 0.5L + 0.5c$ from the wing holder [23], where $L$ is the hinge length and $c$ is the chord length (see Fig. 8.2). The load $P$ causes the wing to pitch through an angle $\eta$. The change of the pitching angle $\Delta\eta$ due to a change of the external load $\Delta P$ is, using a linear spring model, given by

$$\Delta\eta = \frac{\Delta P l_{COL}}{k_{rot}},\tag{8.6}$$

where $k_{rot}$ represents the effective rotational stiffness (see Eq. (8.1)).

Secondly, the change of the interface shear stress $\Delta\tau_{in}$ is discussed. The external load $P$ results in a moment $M$ and a shear force $Q$ (i.e., $Q = P$) at the cross-section of the sticked layers (see Fig. 8.10b). $Q$ is assumed to be constant along the length of the hinge $L$. From ordinary sandwich beam theory, the change of the shear stress $\Delta\tau_{in}$ at a depth $y_i = 0.5t_c + t_d$ (i.e., at the interface) due to a change of the shear force $\Delta Q$ at the cross-section, is given by [1]

$$\Delta\tau_{in}(y_i) = \frac{\Delta Q}{Db}\sum(SE),\tag{8.7}$$

where $D$ represents the flexural rigidity of the entire cross section, $b$ gives the width of the active hinge at the interface, and $\sum (SE)$ represents the sum of the products of the first moment of area $S$ and the Young's modulus $E$ of all parts of the cross section for which $y_c > y_i$. Due to symmetry in the thickness direction, the shear stress at the other interface (i.e., $y_c = -y_i$) is identical.

Finally, given the known voltage-induced $\Delta\tau_{\text{in}}$, the change of the shear force $\Delta Q$ can be obtained from Eq. (8.7). Since $\Delta P = \Delta Q$, the change of the pitching angle $\Delta\eta$ can be determined from Eq. (8.6). This change of the pitching angle gives, consequently, the pitch-duration $\Delta\eta^*$ for which the layers stick.

In conclusion, stick and slip alternate during the pitching motion. The properties of the hinge depend on whether the layers stick or slip as discussed in the next section. Hence, it is important to know the pitch-duration $\Delta\eta^*$ for which the layers stick. This pitch-duration is, in this work, directly related to the change of the friction-induced shear stress $\Delta\tau_{\text{in}}$ using the external load $P$. Hence, this enables the determination of the stick-slip behavior of the active hinge during large deflections.

### 8.3.4 Voltage-Dependent Hinge Properties

The property changes of the active hinge as a function of the applied voltage are twofold: (1) rotational stiffness changes, and (2) energy dissipation changes due to friction at the interfaces. Both influence the passive pitching response.

Depending on whether the layers stick or slip, the tangent rotational stiffness is denoted by

- $k_{\text{rot}}^{\text{st}}$ if the layers stick. In this case, the active hinge consists, basically, of one single bending element, and
- $k_{\text{rot}}^{\text{sl}}$ if the layers slip. In this case, the active hinge consists, basically, of three individually bending layers.

The *tangent* rotational stiffness of the sticking layers is significantly higher compared to the slipping layers case. For example, for a beam consisting of $n$ stacked layers with width $b$ and thickness $t$, the ratio between the second moments of area for sticking and slipping cases is $n^2$ (i.e., $I_{\text{stick}}/I_{\text{slip}} = (n^3 bh^3/12)/(nbh^3/12)$). Subsequently, the *tangent* rotational stiffness is $n^2$ times higher if the layers stick.

For $0 < V < V_{\text{st}}$, the layers sequentially stick and slip during the pitching motion. Whenever the layers slip, energy is dissipated due to friction which leads to mechanical damping. The resulting dissipated power due to friction between the layers (i.e., there are two sliding interfaces in the current hinge design) can be given by

$$P^{\text{fr}}(V, t) = \mu_d \sigma_N (V) b \int_0^L \left( v_1 (\xi, t) + v_2 (\xi, t) \right) d\xi, \qquad (8.8)$$

where $\xi$ represents a coordinate along the active hinge and $v_1 (\xi, t)$ and $v_2 (\xi, t)$ represent the relative velocity between the slipping layers at the upper interface (i.e., at

$y_c = -y_i$, see Fig. 8.10b) and lower interface (i.e., at $y_c = y_i$), respectively. The relative velocity along the hinge is determined by the pitching motion $\eta(t)$ and the thickness of the layers. It is assumed that the relative velocity at the interface increases linearly from zero at the wing holder (i.e., at $\xi = 0$) to its maximal value at the end of the hinge (i.e., at $\xi = L$) although the velocity distribution might be more complex in reality. During slip, the counteracting moment due to the friction can, subsequently, be obtained by

$$M_{x_c}^{\text{fr}} = \begin{cases} 0 & \text{for} \quad V = 0, \\ P^{\text{fr}}(V,t)/\dot{\eta} & \text{for} \quad V \neq 0. \end{cases} \qquad (8.9)$$

Equation (8.9) explicitly assumes that the dissipated power is equal to zero for $V = 0$ although this assumption oversimplifies the occurring slip behavior due to the inevitable normal stress between slipping layers which are jointly bending. This description allows, despite the limitations, to study the influence of an electrostatically controlled active hinge on the passive pitching motion of a flapping wing.

## 8.4   Equation of Motion of Passive Pitching Motion

Since the sweeping motion $\phi(t)$ is prescribed, the rigid wing model involves only one degree of freedom, the pitching angle $\eta$. The equation of motion that governs $\eta$ can be obtained by applying Euler's second law of motion. That is,

$$M_{x_c}^{\text{applied}} + M_{x_c}^{\text{iner}} = 0, \qquad (8.10)$$

where the inertial torque, $M_{x_c}^{\text{iner}}$, in the co-rotating frame is given by

$$M_{x_c}^{\text{iner}} = I_{x_c x_c} \left[ \frac{1}{2} \sin(2\eta)\dot{\phi}^2 - \ddot{\eta} \right] - I_{x_c z_c} \ddot{\phi} \cos(\eta), \qquad (8.11)$$

where $I_{x_c x_c}$ and $I_{x_c z_c}$ are moment of inertia terms. The applied torque, $M_{x_c}^{\text{applied}}$, acting around the pitching axis consists of three components: (i) the elastic torque from the active hinge, $M_{x_c}^{\text{elas}}$, (ii) the voltage-dependent torque due to the friction between the layers, $M_{x_c}^{\text{fr}}$, as calculated by Eq. (8.9), and (iii) the aerodynamic torque $M_{x_c}^{\text{aero}}$.

A quasi-steady aerodynamic model is used to calculate the transient aerodynamic loads. This paper only shows the terms relevant for this work without going into much detail on the specific terms. For more details the reader is referred to [20]. The aerodynamic model assumes the resultant aerodynamic load acting on the wing to be always perpendicular to the chord over the entire stroke (i.e., in $y_c$-direction). For thin plates, this assumption is justified due to a negligible leading-edge suction load and wing surface viscous drag compared to the dominant pressure load. The loads are decomposed into four components as illustrated in Fig. 8.11 and originate from different sources: (1) from the wing translational velocity, leading to $F_{y_c}^{\text{trans}}$ and $M_{y_c}^{\text{trans}}$
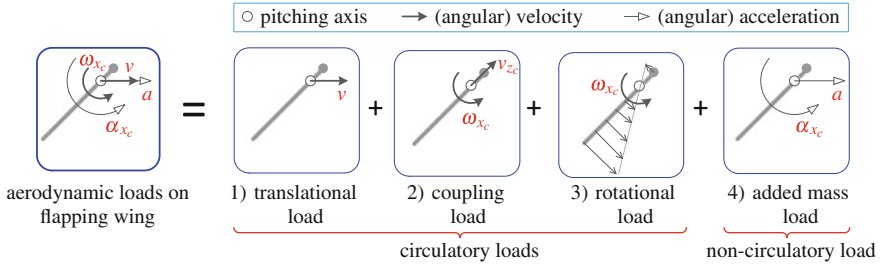
**Fig. 8.11** Decomposition of the flapping wing aerodynamic loads from a quasi-steady model in which $a$ and $v$ are the acceleration and velocity of the wing at the pitching axis, respectively

(see, for example, [14]), (2) from the coupling effect between wing translational and rotational effect, leading to $F_{y_c}^{\mathrm{coupl}}$ and $M_{y_c}^{\mathrm{coupl}}$, (3) from the pure rotational velocity, leading to $F_{y_c}^{\mathrm{rot}}$ and $M_{y_c}^{\mathrm{rot}}$, and (4) from the added mass effect, leading to $F_{y_c}^{\mathrm{am}}$ and $M_{y_c}^{\mathrm{am}}$ (see, for example, [13]). The resultant aerodynamic loads can be calculated by

$$F_{y_c}^{\mathrm{aero}} = \underbrace{-\mathrm{sgn}(\omega_{z_c})\frac{1}{6}\rho_{\mathrm{f}}cR^3 c_{F_{y_c}^{\mathrm{trans}}}(\omega_{y_c}^2 + \omega_{z_c}^2)}_{F_{y_c}^{\mathrm{trans}}} + \underbrace{\frac{3}{8}\pi\rho_{\mathrm{f}}c^2 R^2 \omega_{x_c}\omega_{y_c}}_{F_{y_c}^{\mathrm{coupl}}}$$

$$\underbrace{-\frac{1}{6}\rho_{\mathrm{f}}c^3 RC^{\mathrm{rot}}\omega_{x_c}|\omega_{x_c}|}_{F_{y_c}^{\mathrm{rot}}} + \underbrace{\frac{\pi}{8}\rho_{\mathrm{f}}c^2 R\left[-R(\alpha_{z_c} + \omega_{x_c}\omega_{yc}) - c\alpha_{x_c}\right]}_{F_{y_c}^{\mathrm{am}}},$$

and
$$M_{y_c}^{\mathrm{aero}} = \underbrace{-\mathrm{sgn}(\omega_{z_c})\frac{1}{6}\rho_{\mathrm{f}}c^2 R^3 c_{F_{y_c}^{\mathrm{trans}}}\hat{z}_{cp}^{\mathrm{trans}}(\omega_{y_c}^2 + \omega_{z_c}^2)}_{M_{y_c}^{\mathrm{trans}}}$$

$$+ \underbrace{\frac{3}{32}\pi\rho_{\mathrm{f}}c^3 R^2 \omega_{x_c}\omega_{y_c}}_{M_{y_c}^{\mathrm{coupl}}} - \underbrace{\frac{1}{8}\rho_{\mathrm{f}}c^4 RC^{\mathrm{rot}}\omega_{x_c}|\omega_{x_c}|}_{M_{y_c}^{\mathrm{rot}}}$$

$$+ \underbrace{\frac{\pi}{16}\rho_{\mathrm{f}}c^3 R\left[-R(\alpha_{z_c} + \omega_{x_c}\omega_{yc}) - \frac{9}{8}c\alpha_{x_c}\right]}_{M_{y_c}^{\mathrm{am}}}, \tag{8.12}$$

respectively, where $\rho_{\mathrm{f}}$ is the density of the fluid, $\hat{z}_{cp}^{\mathrm{trans}}$ is the position of the center of pressure due to the translational force which is calculated using an empirical formula (i.e., $\hat{z}_{cp}^{\mathrm{trans}} = 0.261\,(\mathrm{AOA}) + 0.05$), and $C^{\mathrm{rot}}$ is the drag coefficient for a plate revolving at an AOA of 90°. An analytical model proposed by Taha et al. [16] is used to calculate the lift coefficient $c_{F_{y_c}^{\mathrm{trans}}}$ due to the wing translational velocity. This analytical formula provides a good prediction of the lift coefficients of translational flapping wings with different aspect ratios according to the comparison with experimental data from bumble bees, fruit flies and hawk moths.

Eventually, the voltage-dependent equation of motion of the wing passive pitching can be expressed as

$$I_{x_c x_c} \ddot{\eta} + k_{\mathrm{rot}} \eta = M_{y_c}^{\mathrm{aero}} + f(\eta, \dot{\eta}) + M_{x_c}^{\mathrm{fr}} (\dot{\eta}, V), \tag{8.13}$$

where the inertial drive torque $f(\eta, \dot{\eta})$ is given by

$$f(\eta, \dot{\eta}) = \frac{1}{2} I_{x_c x_c} \dot{\phi}^2 \sin(2\eta) - I_{x_c z_c} \ddot{\phi} \cos(\eta). \tag{8.14}$$

Finally, Eq. 8.12 will be used to determine the average lift generated by the flapping wing with the actively controlled elastic hinge. It should be mentioned that the introduced quasi-steady model cannot capture some unsteady effects (e.g., wake capture effect and Wagner effect). Rather good agreements can, however, be found between the results from the quasi-steady model and experiments [20] since the most important unsteady effect (i.e., the prolonged attached of the leading edge vortex) is captured. As such, the model is adequate for this work.

## 8.5   Experimental Analysis

To validate the presented approach on changing the dynamic properties of wing hinges, experiments are done. First, the manufactured wing equipped with an active hinge is discussed together with the experimental setup. After that, the change of the passive pitching motion due to different applied voltages is shown. Finally, the experimentally and analytically obtained results are compared.

### 8.5.1   Realization of Wing with Active Hinge

The wing design consists of three parts: (i) the wing planform, (ii) the active hinge at the wing root, and (iii) the wing holder, see Fig. 8.12. The first part, the wing planform, is composed by gluing two rectangular, 1 mm thick sheets of blue foam (i.e., Expanded PolyStyrene (EPS) with Young's modulus $E_{\mathrm{EPS}} = 3$ GPa) on top of each other. The wingspan $R = 50$ mm and its chord length $c = 20$ mm. The core layer of the active hinge is clamped between these two sheets.

The second part, the active hinge, consists of a conducting core which is on both sides covered by, consecutively, a dielectric layer and a conducting facing. For all conducting layers, spring steel strips are used (i.e., Young's modulus $E_s = 210$ GPa). These spring steel strips are tough and allow for a large number of cyclic, large deflections. The strips have a width $b$ of 12.7 mm and the thickness of the core and the facings is 20 μm and 5 μm, respectively. For the dielectric layers two different approaches can be followed: (1) spin coat a thin polymeric film onto the conducting layer(s) (e.g., the photo-resist SU-8), or (2) use thin sheets of dielectric polymer film (e.g., Mylar). In this work, 5 μm thick Mylar films are tightly attached to the

**(a)**

**(b)**
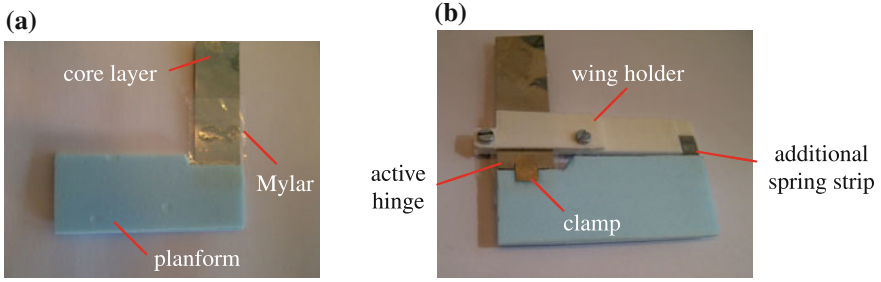


**Fig. 8.12**   Wing design consisting of: (i) the wing planform, (ii) the active hinge, and (iii) the wing holder. **a** Planform with core layer covered by Mylar film. **b** Realized wing design

core conducting layer by gluing its two edges to the spring steel while squeezing the air layer out, see Fig. 8.12a. For the Mylar, the Young's modulus $E_d = 4.25$ GPa, the dielectric constant $\varepsilon_r = 3.25$, the static and dynamic friction coefficients with respect to steel are assumed to be equal, that is, $\mu_s = \mu_d = 0.2$,[1] and the dielectric strength is $V_d = 500$ V/$\mu$m [9, 19]. The total length of the active hinge $L = 5$ mm. To prevent the layer from separating during the pitching motion, clamps are added on both sides. The bending stiffness $EI$ of the blue EPS plate is about $1000\times$ higher in chordwise direction compared to that of the hinge. Therefore, the wing planform can be regarded as a rigid plate.

The third part, the wing holder, is made from 3D-printed plastic. The wing holder is extended over the entire wing span to constrain the movement of the wing tip via a strip of spring steel with a relatively high bending compliance. This constraint prevents warping of the active hinge during large deflections which would lead to undesired large deflections in spanwise direction. The resulting wing design is shown in Fig. 8.12b.

The total mass of the realized wing (excluding the wing holder) is around 300 mg which is relatively high compared to wings found in nature with similar dimensions (e.g., 50 mg) due to glue and the additional clamps. With the currently used layer thicknesses, the ratio between the bending stiffness of the sticked layers, $k_{rot}^{st}$, and the slipping layers, $k_{rot}^{sl}$, is $\left(t_c + 2t_d + 2t_f\right)^3 / \left(t_c^3 + 2t_f^3\right) = 2.34$.

## 8.5.2   *Experimental Setup*

Figure 8.13 shows a picture of the experimental setup as positioned on a vibration-isolating table. The key components of this setup are: (1) the active wing, (2) a non-conducting clamping mechanism to apply the voltage to the facings and to ground

---

[1]Since no appropriate information was found about the friction coefficient between Mylar (PET, Polyethylene terephthalate) and spring steel, the friction coefficient between the similar material PE (Polyethylene) and steel was used instead.
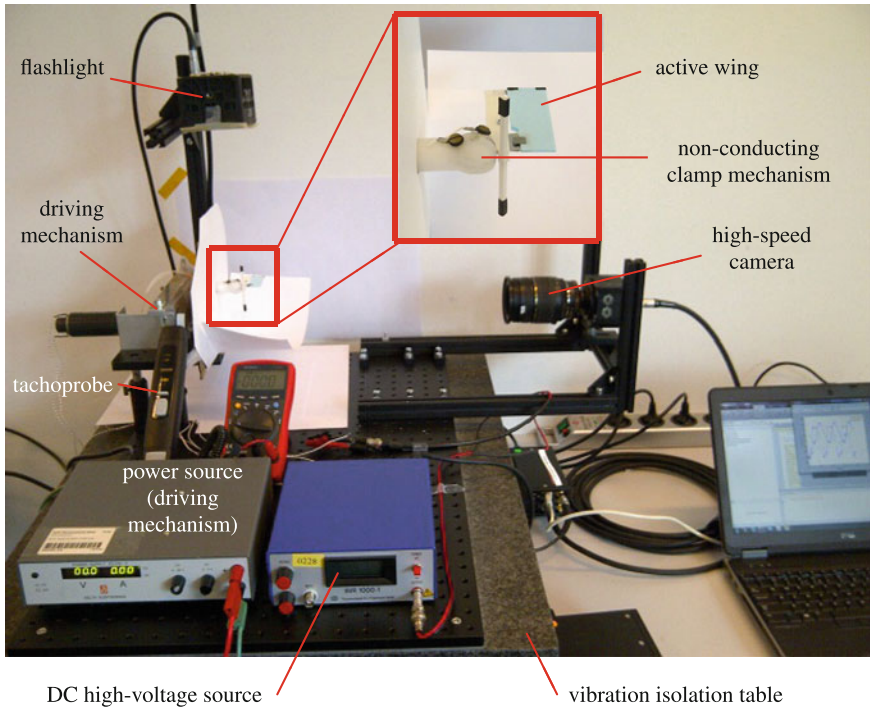
**Fig. 8.13** Experimental setup indicating the key components

the core layer, (3) a DC high-voltage source to apply the voltage to the active hinge, (4) a driving mechanism to enforce a harmonic sweeping motion $\phi(t)$ to the wing, (5) a tachoprobe to measure the driving frequency, and (6) a high-speed camera with a flashlight to capture the flapping motion.

To capture the pitching motion, two black markers are glued onto the wing tip of the wing design in chord-wise direction. The distance on the captured image between these markers when the wing planform is perpendicular to the optical axis of the camera, is taken as the reference length and denoted by $d_b$. The high-speed camera (2000 fps) captures images and, thus, the distance between the black markers during the flapping motion. By relating this distance to the reference length $d_b$, the pitching angle $\eta(t)$ can be calculated.

## 8.5.3 Experimental Results

This section shows experimental results of one specific wing design. Although similar trends were found for other wing designs, this design shows the trend most clearly over a large range of applied voltages. Due to wing fabrication difficulties it was hard
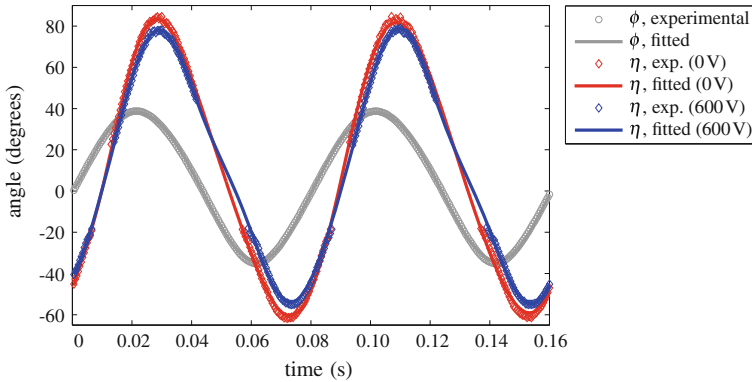
**Fig. 8.14** Lapping kinematics of a passive pitching wing design for which the pitching amplitude decreases if the applied voltage to the active hinge increases

to compare different designs over a large range of applied voltages. These difficulties were, among others, handling the extremely thin spring steel and Mylar sheets (i.e., 5 μm) and preventing a remaining air layer between the stacked layers. This air layer has a negative influence on the voltage-induced normal stress (see Eq. (8.4)). Hence, the number of well succeeded wing designs was limited.

The driving frequency was constant for all experiments and restricted to 12.5 Hz to prevent excessive pitching amplitudes (i.e., $\eta(t) > 90°$). Figure 8.14 shows the resulting flapping kinematics: the sweeping motion $\phi(t)$ and the passive pitching motion $\eta(t)$. The passive pitching motion lags behind the sweeping motion by about 30°. The amplitude of the sweeping motion is 37.5°. The maximum passive pitching angle decreases if the applied voltage to the active hinge increases (i.e., the maximum pitching angle decreases from about 84° for 0 V to about 78° for 600 V) and the phase lag becomes slightly bigger (i.e., a few degrees). The asymmetry of the passive pitching motion is caused by inaccuracies of the realized flapping wing design. The small irregularities or disappearance of measurement points for the pitching motion is caused by the difficulties in tracking the markers on the flapping wing, especially around $\eta(t) = 0°$.

Figure 8.15 shows the change of the average pitching amplitude (using both the maximum and minimum pitching angle) as a function of the applied voltage to the active hinge. To get these results, the flapping frequency was fixed to 12.5 Hz and the applied voltage was increased in steps of 100 V to the maximum of 600 V. For each measurement point, a wait of a couple of seconds was introduced to be assured of steady-state motion before taking images. For some images, the exact location of the black markers was hard to identify. This resulted in a non-smooth pitching angle $\eta(t)$ as shown by some outliers in Fig. 8.14. This, consequently, complicates the determination of the maximum pitching angle. The error bars indicate the uncertainty of the maximum pitching angle as determined by the spread in the measurements.
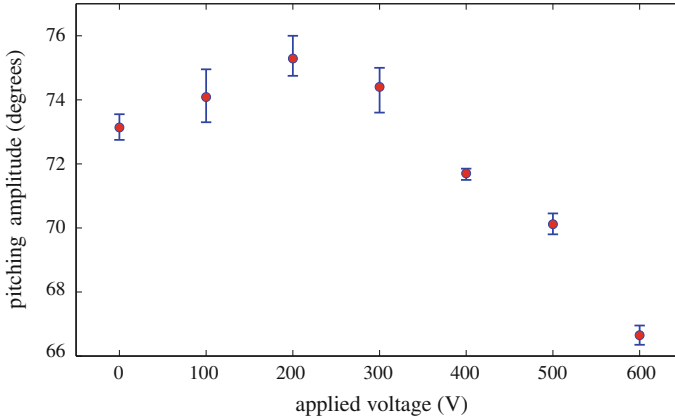
**Fig. 8.15** Average pitching amplitude as a function of the applied voltage $V$. The error bars indicate the measurement uncertainty as determined by the non-smoothness of the measured pitching motion $\eta(t)$

Figure 8.15 shows an increase of the average passive pitching amplitude up to 200 V followed by a monotonic decrease of this amplitude for higher voltages. A possible explanation for this initial amplitude increase is the presence of the clamps on the wings to keep the layers from separating. The friction between these clamps and the outer facings decreases if the voltage-induced sticking of the stacked layers increases. The reduction of friction reduces the energy loss and, hence, increases the average pitching amplitude.

The targeted gap between the core conducting layer and the outer facings was 5 μm as determined by the thickness of the Mylar sheet. Since the electric strength of Mylar is 500 V/μm, the maximum possible applied voltage to the active hinge is, theoretically, restricted to 2500 V. Figures 8.14 and 8.15 show only results up to 600 V since the hinge failed for higher voltages. This could have several reasons, for example: (i) due to Mylar sheet irregularities (e.g., a small scratch) the practical dielectric strength is lower than the theoretical value, or (ii) due to the presence of the very thin air gap between the conducting layers and the dielectric sheet. If the breakthrough voltage of the air gap is reached, a current is going to flow which might locally burn the dielectric Mylar layer.

## 8.6 Numerical Analysis and Comparison to Experimental Results

The numerical analysis to determine the passive pitching motion is complicated by the abrupt jump in the hinge stiffness if the layers of the active hinge change from stick to slip, or visa versa. To solve this problem the jump of the hinge stiffness is
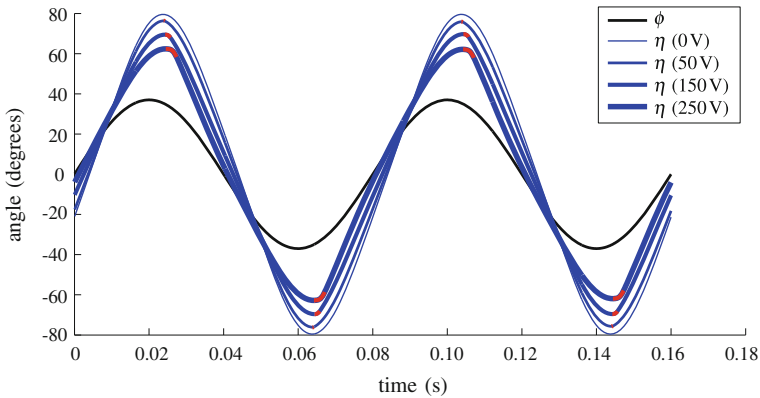
**Fig. 8.16** Numerical results of the flapping kinematics for different applied voltages to the active hinge. Segments in *red* show the pitch-duration $\Delta\eta^*$ (i.e., just after the maximum pitching angle) for which the layers stick

smoothed by a $C^\infty$ function, and the ode15s solver from Matlab® is used to solve this stiff problem. Figure 8.16 shows the sweeping motion $\phi(t)$ and numerical steady-state passive pitching $\eta(t)$ for different applied voltages $V$ to the active hinge. The figure clearly shows the decrease in the pitching amplitude for an increase of the voltage. The passive pitching motion without voltage (i.e., 0 V) lags behind the sweeping motion by about 30°, which is comparable to the experimental results. The phase lag increases slightly if the voltage increases. Additionally, the figure indicates the locations at which the layers stick (i.e., just after the maximum pitching angle). The pitch-duration $\Delta\eta^*$ for which the layers stick increases if the applied voltage increases although it remains relatively short with respect to the entire flapping cycle.

Figure 8.17 shows the numerical change of the average pitching amplitudes as a function of the applied voltages. The average pitching angle decreases monotonically, almost linearly, if the voltage increases. The cycle-average lift force decreases accordingly, see Fig. 8.18. The average lift force decreases by about 31 % if the voltage is increased from 0 to 250 V, which is sufficient in controlling lightweight FWMAV designs. The maximum applied voltage is set to 250 V. For voltages higher than 250 V, the passive pitching motion $\eta(t)$, as shown in Fig. 8.16, starts to deviate significantly from being harmonic. Additionally, the convergence becomes poor such that a steady-state solution can not be found.

The numerical passive pitching amplitude change due to the applied voltage (i.e., Figs. 8.16 and 8.17) is more significant compared to the experimental results of Figs. 8.14 and 8.15 although the trend is similar (i.e., decreasing amplitude and increasing phase lag when the applied voltage increases). The discrepancy can be explained by: (1) the simplifying assumptions in the theoretical model, (2) the difficulties in the manufacturing process, and (3) the presence of additional air between the conducting layers and the Mylar.

**Fig. 8.17** Numerical
average passive pitching
amplitudes as a function of
the applied voltages
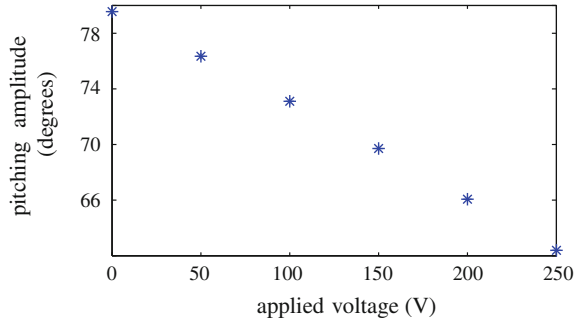


**Fig. 8.18** Numerical
average lift force as a
function of the applied
voltages
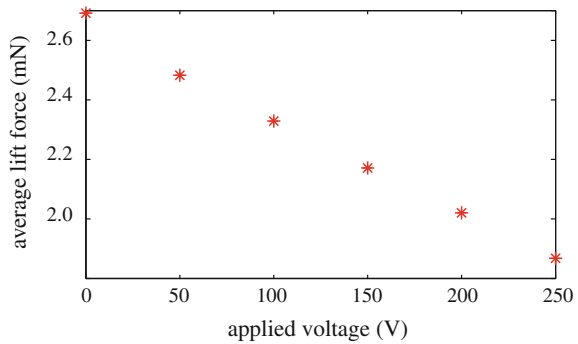


## 8.7   Conclusions and Recommendations

This paper presents a method to actively control the passive pitching motion of a
flapping wing using electrostatic sticking of stacked layers. These stacked layers con-
stitute the elastic hinge at the wing root in a FWMAV design. Actively modifying
the structural properties of that hinge (e.g., damping and stiffness) results in signifi-
cant changes of the wing' passive pitching motion and, hence, of its lift production.
The hinge in this work consists of three conducting spring steel layers which are
separated from each other by dielectric Mylar films.

During the pitching motion, the layers, consecutively, stick and slip with respect
to each other. The layers stick due to the voltage-induced normal stress between the
layers. Whenever the layers stick, the bending stiffness of the hinge is significantly
higher compared to the case when the layers slip (i.e., $2.34 \times$ for our hinge). If the
layers slip, power is dissipated due to friction which is induced by the normal stress
between the layers. This friction results in an additional moment that dampens the
passive pitching motion.

Numerical simulations show significant changes of the pitching amplitude if the
applied voltage to the active hinge increases. The pitch-duration for which the layers
stick increases with the applied voltage, although it remains relatively short com-
pared to the duration for which the layers slip. The resulting average lift force changes

corresponding to the different applied voltages are sufficient for control purposes of lightweight FWMAV designs. The theoretical model gives, despite the introduced limitations, a clear insight into the voltage-controlled stick-slip behavior of the active hinge during large deflections.

Experiments are conducted to study the practical applicability of this active elastic hinge for small-scale and lightweight FWMAV applications. To obtain experimental results, several fabrication difficulties have been tackled, for example, the handling of the very thin Mylar films (i.e., $5\,\mu m$). The experimental results show, although suppressed, the same trends compared to the numerical simulations. The results are less significant, mainly due to: (1) the presence of an air layer between the conducting layers and the dielectric layers, (2) the presence of Mylar film irregularities. Despite of these shortcomings, the results clearly show a decrease of the pitching amplitude as a function of the applied voltage. Hence, it shows the potential of this method to control FWMAVs.

In future work, the numerical model might be improved to model the stick-slip behavior of the active hinge more accurately (e.g., the friction between the layers in the absence of a control voltage). Additionally, long lasting experiments need to be conducted to study the influence of wear due to friction between the Mylar and the conducting sheets. Alternatively, it is interesting to change the applied voltage during a flapping cycle and study the occurring transient behavior. The fabrication process can be optimized by preparing jigs or well-designed tools.

# References

1. Allen H (1969) Analysis and design of structural sandwich panals. Pergamon Press, Oxford
2. Bergamini A, Christen RX, Maag B, Motavalli M (2006) A sandwich beam with electrostatically tunable bending stiffness. Smart Mater Struct 15(3):678–686. doi:10.1088/0964-1726/15/3/002
3. Bolsman CT, Goosen JFL, van Keulen F (2009) Design overview of a resonant wing actuation mechanism for application in flapping wing mavs. Int J Micro Air Veh 1(4):263–272. doi:10.1260/175682909790291500
4. Clark WW (2000) Vibration control with state-switched piezoelectric materials. J Intell Mater Syst Struct 11(4):263–271. doi:10.1106/18CE-77K4-DYMG-RKBB
5. de Croon G, de Clercq K, Ruijsink R, Remes B, de Wagter C (2009) Design, aerodynamics, and vision-based control of the delfly. Int J Micro Air Veh 1(2). doi:10.1260/175682909789498288
6. Dudley R (2000) The biomechanics of insect flight: form, function, evolution. Princeton University Press
7. Finio BM, Wood RJ (2012) Open-loop roll, pitch and yaw torques for a robotic bee. In: IEEE International conference on intelligent robots and systems, pp. 113–119. doi:10.1109/IROS.2012.6385519. Art. no. 6385519
8. Ford C, Babinsky H (2014) Impulsively started flat plate circulation. AIAA J 52(8):1800–1802
9. Free Flight Supplies (2015). www.freeflightsupplies.co.uk/mylarspec.pdf

10. Howell LL (2001) Compliant Mechanisms. Wiley
11. Ma KY, Felton SM, Wood RJ (2012) Design, fabrication, and modeling of the split actuator microrobotic bee. In: IEEE international conference on intelligent robots and systems, pp. 1133–1140. doi:10.1109/IROS.2012.6386192. Art. no. 6386192
12. Majidi C, Wood RJ (2010) Tunable elastic stiffness with micro confined magnetorheological domains at low magnetic field. Appl Phys Lett 97(16). http://dx.doi.org/10.1063/1.3503969. Art. no. 164104
13. Newman J (1977) Marine hydrodynamics. The MIT Press
14. Sane SP, H, DM (2002) The aerodynamic effects of wing rotation and a revised quasi-steady model of flapping flight. J Exp Biol 205(8):1087–1096. http://jeb.biologists.org/content/205/8/1087.short
15. Tabata O, Konishi S, Cusin P, Ito Y, Kawai F, Hirai S, Kawamura S (2001) Micro fabricated tunable bending stiffness devices. Sens Actuators, A 89(1–2):119–123. doi:10.1016/S0924-4247(00)00538-0
16. Taha HE, Hajj MR, Beran PS (2014) State-space representation of the unsteady aerodynamics of flapping flight. Aerosp Sci Technol 34:1–11. doi:10.1016/j.ast.2014.01.011
17. Teoh ZE, Fuller SB, Chirarattananon P, Prez-Arancibia NO, Greenberg JD, Wood RJ (2012) A hovering flapping-wing microrobot with altitude control and passive upright stability. In: IEEE international conference on intelligent robots and systems, pp. 3209–3216. doi:10.1109/IROS.2012.6386151
18. Teoh ZE, Wood RJ (2014) A bioinspired approach to torque control in an insect-sized flapping-wing robot. In: Proceedings of the IEEE RAS and EMBS international conference on biomedical robotics and biomechatronics, pp. 911–917. doi:10.1109/BIOROB.2014.6913897. Art. no. 6913897
19. Toolbox TE (2015). http://www.engineeringtoolbox.com/friction-coefficients-d_778.html
20. Wang Q, Goosen JFL, van Keulen F (2016) A predictive quasi-steady model of aerodynamic loads on flapping wings. J Fluid Mech 800:688–719
21. Wood R (2007) Design, fabrication, and analysis of a 3dof, 3cm flapping-wing mav. In: IEEE/RSJ international conference on intelligent robots and systems, 2007. IROS 2007, pp. 1576–1581. doi:10.1109/IROS.2007.4399495
22. Wood RJ (2008) The first takeoff of a biologically inspired at-scale robotic insect. IEEE Trans Robot 24(2):341–347. doi:10.1109/TRO.2008.916997
23. Zhao L, Huang Q, Deng X, Sane SP (2010) Aerodynamic effects of flexibility in flapping wings. J R Soc Interface 7:44. doi:10.1098/rsif.2009.0200